Journal of Alloys and Compounds 509 (2011) 8720–8727

Contents lists available at ScienceDirect

Journal of Alloys and Compounds

journal homepage: www.elsevier.com/locate/jallcom

Comparative study of $Ce_{0.85}Sm_{0.075}Nd_{0.075}O_{2-\delta}$ electrolyte synthesized by different routes

Zhan Gao[a,b], Xingmin Liu[b], Bill Bergman[a], Zhe Zhao[a,b,*]

[a] Department of Materials Science and Engineering, Royal Institute of Technology (KTH), SE 10044 Stockholm, Sweden
[b] Department of Materials and Environmental Chemistry, Arrhenius Laboratory, Stockholm University, SE 10691 Stockholm, Sweden

ARTICLE INFO

Article history:
Received 8 March 2011
Received in revised form 8 June 2011
Accepted 13 June 2011
Available online 17 June 2011

Keywords:
Solid oxide fuel cells
Electrolyte
Co-doped
Ceria
Conductivity

ABSTRACT

In this work, four different methods, including polyvinyl alcohol (PVA)-assisted sol–gel process, polyethylene glycol (PEG)-assisted sol–gel process, citrate sol–gel process and oxalate coprecipitation process (OCP) are employed to synthesize the Sm and Nd co-doped ceria electrolyte with the composition of $Ce_{0.85}Sm_{0.075}Nd_{0.075}O_{2-\delta}$ (SNDC). The phase structure of the powders can be well indexed with the fluorite-type CeO_2 structure. The morphology of sintered samples indicates that the ceramics can be highly densified. The relative density and the average grain size vary with the synthesis processes and the sintering temperatures. The bulk conductivities are quite close and the OCP–SNDC yields highest grain-boundary conductivities and total conductivities. The results indicate that the OCP process for the powder synthesis results in higher relative density and conductivities, lower grain-boundary resistance and activation energy. Grain-boundary space charge potentials for different specimens are calculated based on the Mott–Schottky model. The synthesis process and sintering temperature have significant effect on the space charge potential and the specific grain-boundary conductivity.

1. Introduction

Low-temperature solid oxide fuel cell (SOFC) has collected a great deal of attention during the last decade since it can allow more flexible material selection, reduced fabrication cost, better sealing and prolonged lifetime, which could highly facilitate the commercialization process of SOFCs [1]. Among varieties of electrolytes, doped ceria possesses immense potential in view of its relatively high conductivity in the low-temperature range. Gd-doped ceria and Sm-doped ceria have been widely investigated and they have been substantiated to perform better conductivity than other trivalent lanthanide-doped ceria [2,3]. However, doped ceria suffers from the electronic conduction under low oxygen partial pressure and high grain-boundary resistivity. Co-doping strategies and optimized synthesis process have been utilized to modify the structure and enhance the conductivity of ceria-based electrolyte.

It has been well recognized that the total conductivity of polycrystalline doped ceria is determined by both the grain bulk conductivity and the grain-boundary conductivity. Co-doping technique with rare earth or alkaline earth ion has been widely recognized as an effective method to further improve the conductivity of singly doped ceria. A variety of co-doping systems, including Sm^{3+} and Nd^{3+} [4], Lu^{3+} and Nd^{3+} [5], Eu^{3+} and Sr^{2+} [6], Gd^{3+} and Sm^{3+} [7], Sm^{3+} and Ca^{2+} [8], Y^{3+} and Dy^{2+} [9], have been extensively investigated. Omar et al. [5] investigated the Lu and Nd co-doped ceria electrolyte ($Lu_xNd_yCe_{1-x-y}O_{2-\delta}$) based on the concept of critical dopant ionic radius. The elastic strain is negligible since the positive elastic strain from Nd^{3+} is compensated by the negative elastic strain from Lu^{3+}. The variation trend of elastic strain is in accordance with the conductivity for different compositions, indicating elastic strain is one considerable factor to design electrolytes with enhanced ionic conductivity, since the elastic strain is closely associated with critical dopant ionic radius. According to density function theory, the effective atomic number of the ideal dopant for the lanthanide elements is assumed to be between 61 (Pm) and 62 (Sm) [10], which can be constructed using Sm and Nd co-doping into ceria. It was shown that the grain ionic conductivity of $Ce_{0.85}Sm_{0.075}Nd_{0.075}O_{2-\delta}$ is 30% higher than that of $Ce_{0.9}Gd_{0.1}O_{2-\delta}$ at 550 °C [4]. The maximum power density

* Corresponding author at: Department of Materials Science and Engineering, Royal Institute of Technology (KTH), SE 10044 Stockholm, Sweden.
Tel.: +46 08 7908381.
E-mail address: zhezhao@kth.se (Z. Zhao).

0925-8388/$ – see front matter © 2011 Elsevier B.V. All rights reserved.
doi:10.1016/j.jallcom.2011.06.040

of the anode supported fuel cell using $Ce_{0.85}Sm_{0.075}Nd_{0.075}O_{2-\delta}$ as electrolyte (thickness 10 μm) reaches 1.43 W cm^{-2} at 650 °C, indicating $Ce_{0.85}Sm_{0.075}Nd_{0.075}O_{2-\delta}$ is a promising electrolyte for low-temperature SOFCs [11].

Previous research has validated that the grain-boundary resistance always plays a dominant role in the total conductivity of the electrolyte. The grain-boundary conductivity is closely associated with the impurity and the microstructure of the grain boundary, which are mainly influenced by the synthesis routes of powder, according to the Bauerle model [12]. A lot of routes have been devoted to synthesize the co-doped ceria powder, such as solid-state reaction technique [4], precipitation technique [13], sol–gel technique [14], hydrothermal technique [14], glycine–nitrate combustion technique [15], and others. However, there is lack of information on how the processing route of powder influences the ionic conductivity of the ceramics.

In this work, four different processes have been utilized to synthesize the $Ce_{0.85}Sm_{0.075}Nd_{0.075}O_{2-\delta}$ (SNDC) electrolyte. The effect of different synthesis process on the microstructure and ionic conductivity has been investigated.

2. Experimental

2.1. Synthesis

$Ce(NO_3)_3{\cdot}6H_2O$ (99.9%, Alfa Aesar), $Sm(NO_3)_3{\cdot}6H_2O$ (99.9%, Alfa Aesar) and $Nd(NO_3)_3{\cdot}6H_2O$ (99.9%, Alfa Aesar) were selected as the starting materials for all the synthesis processes. The $Ce_{0.85}Sm_{0.075}Nd_{0.075}O_{2-\delta}$ powders were synthesized by four different methods, respectively.

2.1.1. Polyvinyl alcohol (PVA)-assisted sol–gel process

The PVA-assisted sol–gel method was designated as PVA–SNDC. PVA (VWR International Ltd., Sweden) was dissolved in water under heating and stirring to form 5 wt.% PVA solution. Stoichiometric $Ce(NO_3)_3{\cdot}6H_2O$, $Sm(NO_3)_3{\cdot}6H_2O$ and $Nd(NO_3)_3{\cdot}6H_2O$ were dissolved in the distilled water, followed by the addition of PVA solution under heating and stirring. The mole ratio of –OH in the PVA to the metal cations was controlled to be 1:1. The pH value of the solution was adjusted to be *ca.* 7.0 using diluted nitric acid and ammonium solution. The above solution was heated on the hot plate at 80 °C to evaporate the excess water. It turned to be a viscous and transparent sol. The solid gel can be obtained by further heating the sol. It was annealed in a muffle furnace at 250 °C for 6 h. The obtained precursor powder was finally annealed at 700 °C for 2 h.

2.1.2. Polyethylene glycol (PEG)-assisted sol–gel process

The PEG-assisted sol–gel method was designated as PEG–SNDC. The synthesis process was same with the PVA-assisted sol–gel method, except that the PVA was replaced by the PEG (Alfa Aesar). The mole ratio of –OH in the PEG to metal cations was controlled to be 1:1. Both the PVA and PEG act as complexant and fuel in the synthesis process.

2.1.3. Citrite sol–gel process

The citrite sol–gel method was designated as C–SNDC. Citric acid (99%, Alfa Aesar) was dissolved in water under heating and stirring. Stoichiometric $Ce(NO_3)_3{\cdot}6H_2O$, $Sm(NO_3)_3{\cdot}6H_2O$ and $Nd(NO_3)_3{\cdot}6H_2O$ were dissolved in the distilled water, followed by the addition of citric acid solution under stirring. The mole ratio of citric acid to total metal ions was controlled to be 1.5:1 in the precursor solution. Gel was obtained after evaporating the water at 80 °C. The gel was annealed in a muffle furnace at 250 °C for 6 h. It turned into a black viscous mass and then burned. All the resulting shallow-yellowish ashes were treated at 700 °C for 2 h in muffle furnace to remove the carbon residues and form a well crystalline structure.

2.1.4. Oxalate coprecipitation process

The fourth powder was synthesized by an oxalate coprecipitation method, which was designated as OCP–SNDC. The stoichiometric starting materials were dissolved in the distilled water, and then dripped to the oxalic acid solution, which was adjusted to neutral pH (6.6–6.9) by dilute ammonia solution. Calcination took place at 700 °C for 2 h after the precipitate was fully washed by water and ethanol.

The synthesis processes were carefully optimized to minimize the element loss and ensure the final chemical compositions in the four powders are almost the same, which was certified by the X-ray fluorescence (XRF 1800).

SNDC pellets with about 10 mm in diameter and 1 mm in thickness were prepared by uniaxially pressing of SNDC powder and sintering at 1400 °C, 1500 °C and 1600 °C for 5 h, respectively. For the morphology characterization of grain and grain boundaries, the sintered pellets were polished and thermally etched at 100 °C lower temperature than the sintering temperature for 30 min.

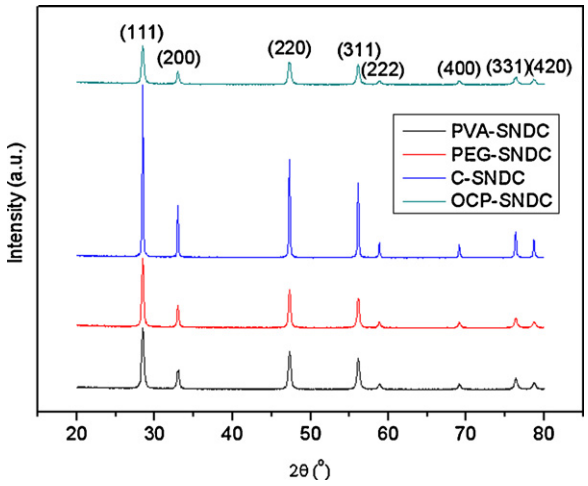

Fig. 1. Room-temperature XRD patterns for SNDC derived from different routes after being annealed at 700 °C for 2 h.

2.2. Characterizations

The conductivity was performed by the a.c. impedance spectroscopy method from 700 °C to 200 °C (SI 1260 Solartron Impedance/Gain-Phase Analyzer) with a frequency range of 100 mHz to 100 kHz using an excitation voltage of 10 mV under open circuit voltage state. Au paste was brushed on both surfaces of the pellet, which is followed annealing at 800 °C for 30 min. The phase structure was detected by the XRD (PANalytical X'pert Pro). The unit cell parameters were determined by Rietveld fit of the XRD patterns using PowderCell 2.4 program [16]. The morphology and microstructural studies of the powders and pellets were performed by scanning electron microscope (SEM, JSM-7000F, JEOL Ltd., Japan) and TEM (JEOL 2100LaB6).

3. Results and discussion

Fig. 1 presents the XRD profiles of the calcined SNDC powders measured at room temperature. It can be observed that all the patterns are single phase with a cubic fluorite structure. The lattice parameters for the PVA–SNDC, PEG–SNDC, C–SNDC, OCP–SNDC are 5.4349 Å, 5.4357 Å, 5.434 Å, 5.4354 Å, respectively. The lattice parameters for different powders are quite close, but a small discrepancy can be observed. It might be related to the different doping amounts in the lattice, resulting from different segregation amounts of Sm and Nd on the grain boundaries in different synthesis processes. The lattice parameters are higher than the value of 5.411 Å for the pure CeO_2 (JCPDS No. 04-0593). The lattice expansion can be ascribed to the larger ionic radius of Sm^{3+} (0.1079 nm) and Nd^{3+} (0.1109 nm) than that of Ce^{4+} (0.097 nm) for a VIII coordination [17].

Fig. 2a shows the typical morphology of the OCP–SNDC powder. The particles take on pseudo-spherical shape from 20 nm to 40 nm in diameter. The particles form agglomerates. The insert in Fig. 2a demonstrates a selected area electron diffraction pattern, which is in accordance with the cubic fluorite CeO_2 crystalline structure based on the JCPDS (No. 04-0593) standard. The eight broad rings correspond to the (111), (200), (220), (311), (222), (400), (331) and (420) reflections of the cubic CeO_2 structure. The HRTEM image for a single particle is shown in Fig. 2b. The distance between adjacent fringes is approximately 0.313 nm, which is similar to the d-spacing of the (111) plane of the CeO_2 standard (0.31234 nm).

Fig. 3a–d presents the micrographs of the powders derived from different preparation processes. The derived PVA–SNDC powder is nanometric in size. PVA–SNDC powder takes on strong agglomeration with clusters of about 0.3–5 μm. The PEG–SNDC powder appears similar morphology with the PVA–SNDC powder since the precursor of PEG and PVA possess similar polymeric structure.

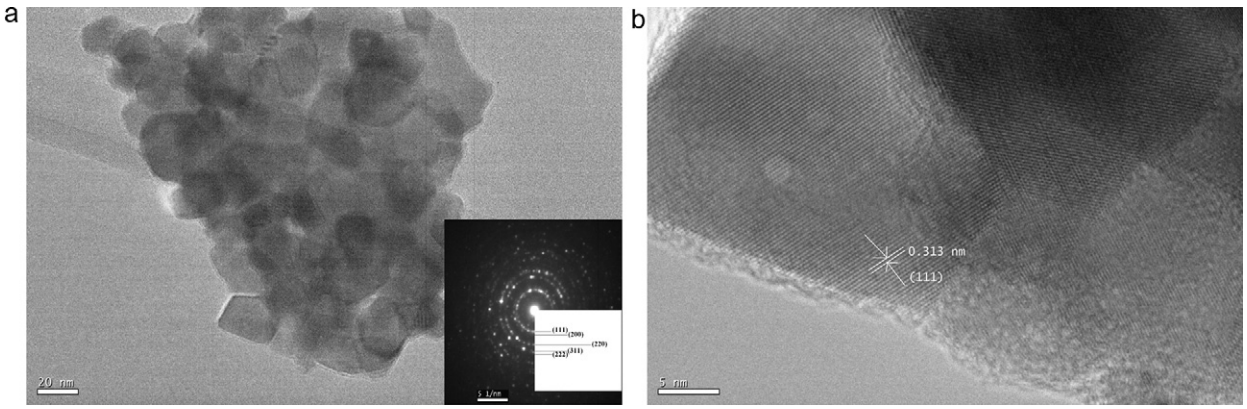

Fig. 2. (a) Typical morphology and selected area electron diffraction pattern (insert) of OCP–SNDC powder calcined at 700 °C for 2 h. (b) HRTEM image of OCP–SNDC powder calcined at 700 °C for 2 h.

PEG and PVA act as templates in the powder synthesis process. As shown in Fig. 3c, the C–SNDC particles are nanometric and form less agglomeration in comparison with the PVA–SNDC and PEG–SNDC particles, which can be ascribed to the fact that the molecular weight and chain length of polymer formed by the citric acid was much smaller than that of PVA and PEG, since all of them act as complexant in the synthesis process. The OCP–SNDC particles appear rod and flake-like shape. The different morphologies of SNDC powders might have great effect on the properties of green compacts.

Fig. 4a–d shows the typical micrographs of the pellets originated from different synthesis methods sintered under the same condition. The average grain sizes of the etched samples are obtained using the linear intercept technique [18], which are shown in Table 1. The OCP–SNDC yields the highest relative density, while the relative densities of the other SNDC are quite close, indicating that the OCP–SNDC has superior sinterability.

Fig. 4d–f presents the micrographs of the OCP–SNDC pellet sintered at different temperatures. The pores are reduced with the increasing sintering temperatures, indicating the relative density is enhanced, which is in accordance with the results displayed in Table 2. The average grain size of the OCP–SNDC pellet sintered at 1400 °C, 1500 °C and 1600 °C is 1.19 μm, 1.21 μm and 4.12 μm, respectively, which becomes larger.

Fig. 5 presents the typical plots of impedance for the SNDC derived from different synthesis processes measured at 300 °C.

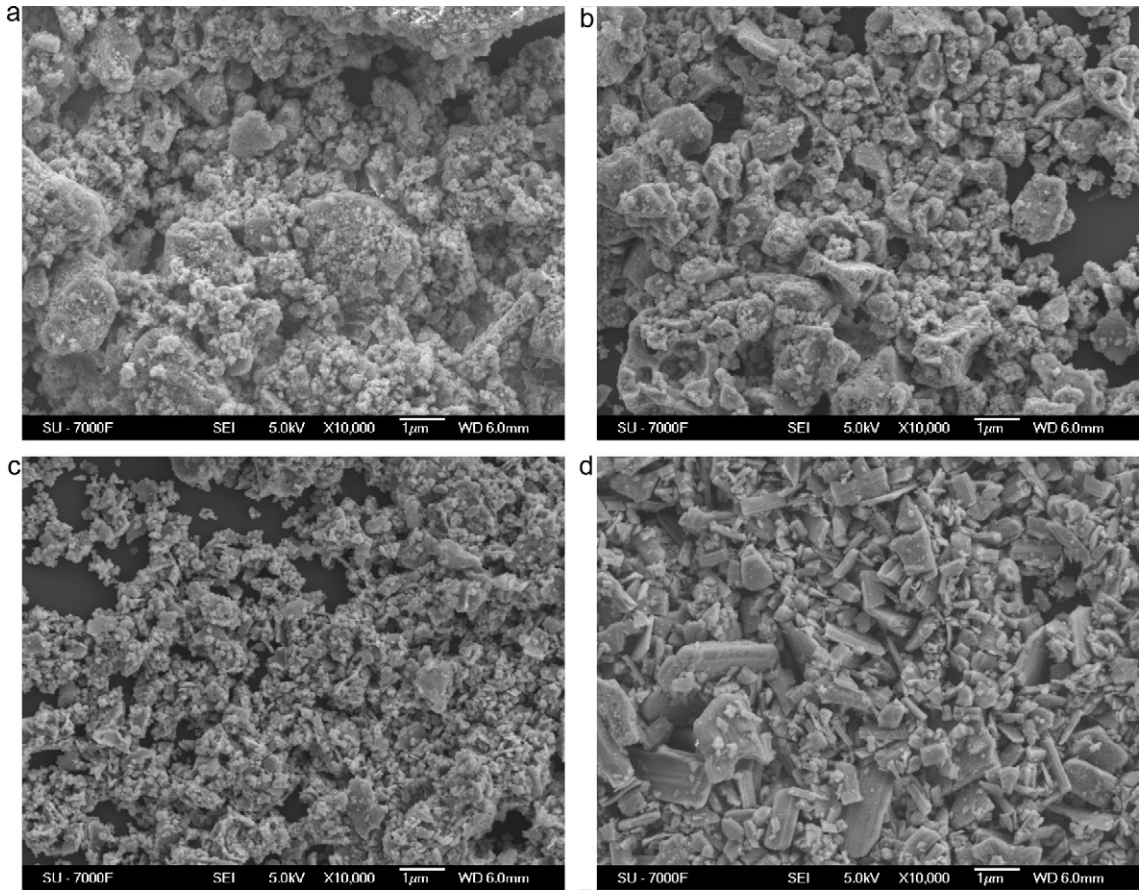

Fig. 3. SEM images of SNDC powder calcined at 700 °C for 2 h: (a) PVA–SNDC, (b) PEG–SNDC, (c) C–SNDC and (d) OCP–SNDC.

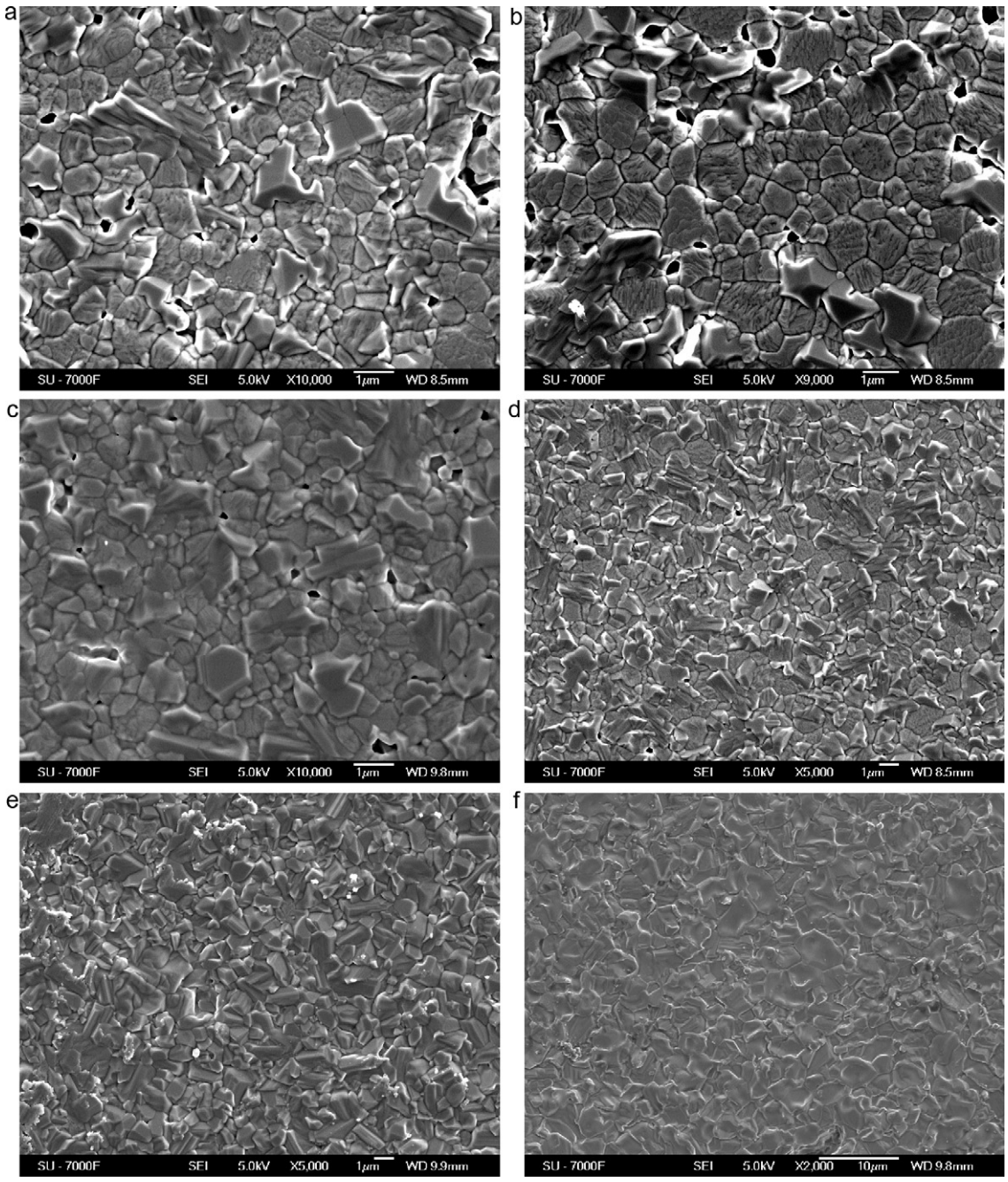

Fig. 4. SEM images of the surface of SNDC sintered pellets: (a) PVA–SNDC pellet sintered at 1400 °C for 5 h, (b) PEG–SNDC pellet sintered at 1400 °C for 5 h, (c) C–SNDC pellet sintered at 1400 °C for 5 h, (d) OCP–SNDC pellet sintered at 1400 °C for 5 h, (e) OCP–SNDC pellet sintered at 1500 °C for 5 h and (f) OCP–SNDC pellet sintered at 1600 °C for 5 h.

The plots can be modeled by the equivalent circuit with the configuration of $L_1(R_1CPE_1)(R_2CPE_2)(R_3CPE_3)$, in which L_1 represents the inductor, R is the resistor and CPE corresponds to the constant phase element. Three different contributions can be clearly distinguished in the investigated frequency range. The high-frequency arc, corresponding to the equivalent circuit model with a resistor R_1 and a constant phase element CPE_1, can be ascribed to the grain bulk properties. The medium-frequency arc relates to the grain-boundary properties represented by a resistor R_2 and a constant phase element CPE_2 in the equivalent circuit model. The

Table 1
Relative densities and average grain sizes for the SNDC pellets synthesized via different routes sintered at 1400 °C.

	PVA–SNDC	PEG–SNDC	C–SNDC	OCP–SNDC
Relative density (%)	93.69	92.15	92.87	96.2
Average grain size (μm)	1.09	1.21	1.03	1.19
Activation energy E_a/eV (bulk)	0.725	0.7455	0.7539	0.7005
Activation energy E_a/eV (grain boundary)	1.0342	1.0356	1.0097	0.9864
Activation energy E_a/eV (total)	0.9575	0.9679	0.9486	0.9146

Table 2
Relative densities and average grain sizes for OCP–SNDC pellets sintered at different temperatures.

	Sintering temperature (°C)		
	1400	1500	1600
Relative density (%)	96.2	97.72	98.15
Average grain size (μm)	1.19	1.21	4.12

low-frequency arc is attributed to the electrode process described by the parallel arrangement of a resistor R_3 and a constant phase element CPE_3. As shown in Fig. 5, the OCP–SNDC yields the lowest grain-boundary resistance.

The individual conductivity σ_i can be converted from the corresponding resistance R_i according to the following equation:

$$\sigma_i = \frac{l}{R_i S} \quad (1)$$

where l is the thickness of the pellets and S is the effective area of the sample. The bulk conductivity and grain-boundary conductivity can be obtained from the equation. Fig. 6 shows the temperature dependence of conductivities plots for SNDC originated from different synthesis procedure sintered at 1400 °C for 5 h. The bulk conductivities are quite similar, since the bulk conductivities are mainly determined by the sample composition. The results indicate that the sample compositions scarcely vary with the synthesis procedures. However, a decrease in bulk conductivity of C–SNDC can be observed at high temperatures, since C–SNDC might probably possess higher migration enthalpy of oxygen ions than other specimens [19]. The OCP–SNDC has the highest grain-boundary conductivities, which can be ascribed to the well densified samples as shown in Fig. 4d. The grain-boundary conductivities of PVA–SNDC and PEG–SNDC are quite close, much higher than those of the C–SNDC. The SiO_2 contamination can be always observed on the grain boundary, which is from the ceramic process and sintering. SiO_2 contamination might be from the glass container where the high temperature combustion was executed. The impurity is assumed to be the least for the OCP process in comparison with the other processes since the high temperature combustion was not carried out in the OCP process. From the microstructure perspective, the OCP–SNDC might contain more continuous grain-boundary phases, which can also facilitate the grain-boundary conductivity. In the Sm and Nd co-doped ceria, Sm is observed to segregate to the grain boundaries [20]. The segregation amount of Sm is assumed to be closely related to the synthesis process. Higher segregation results in the lower grain-boundary conductivities. The amount of Sm segregating to grain boundary for the C–SNDC specimen might be higher than those of others. Sm cations accumulate at the grain boundaries due to elastic strain and Coulomb interaction. The highest grain-boundary conductivities of OCP–SNDC might be related to the lowest amount of segregation of Sm cations. Obviously, both the amount of Sm

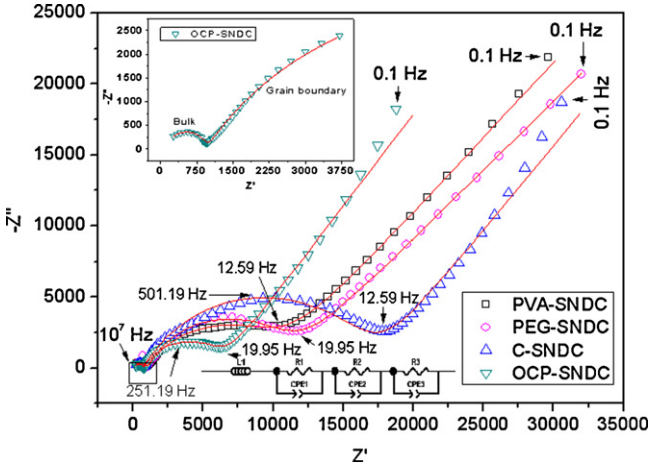

Fig. 5. Typical impedance spectrum of SNDC ceramic measured in air at 300 °C, the dots are the original data and the lines are the modeling data; insert: equivalent circuit utilized to model the impedance spectrum.

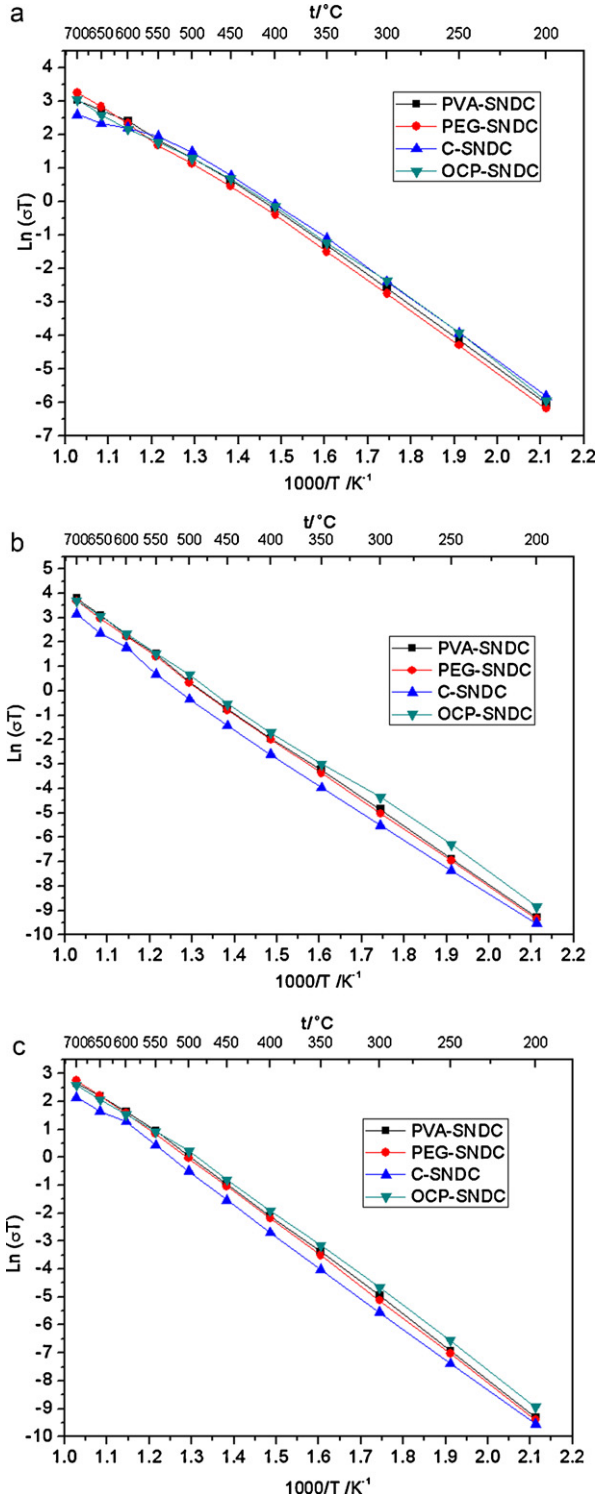

Fig. 6. (a) Bulk, (b) grain-boundary and (c) total conductivity of different SNDC pellets sintered at 1400 °C.

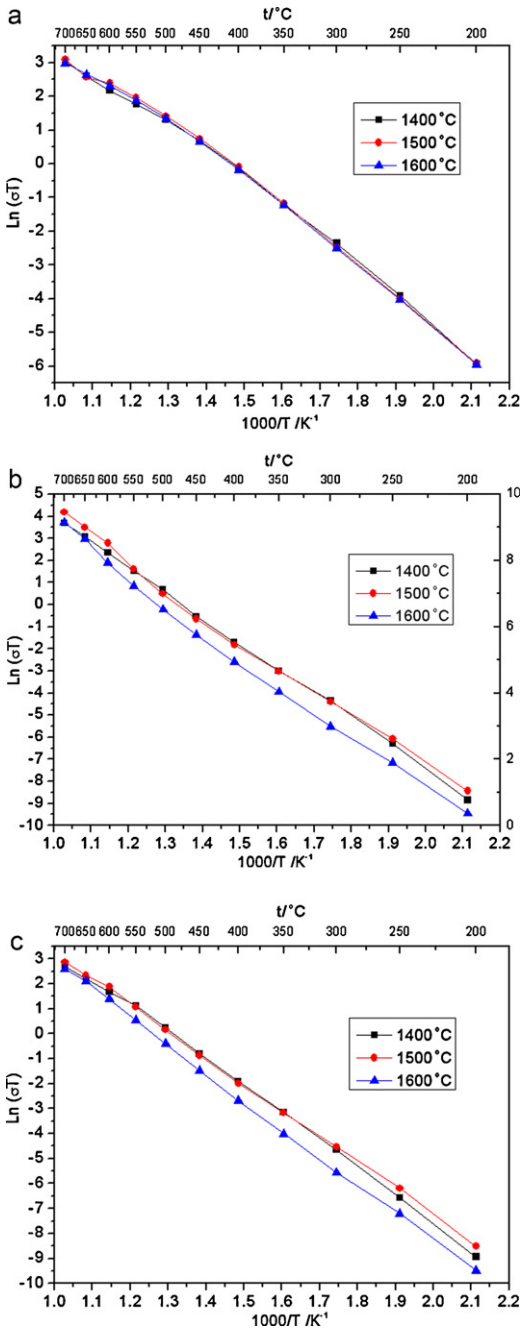

Fig. 7. (a) Bulk, (b) grain-boundary and (c) total conductivity of OCP–SNDC sintered at 1400 °C, 1500 °C and 1600 °C.

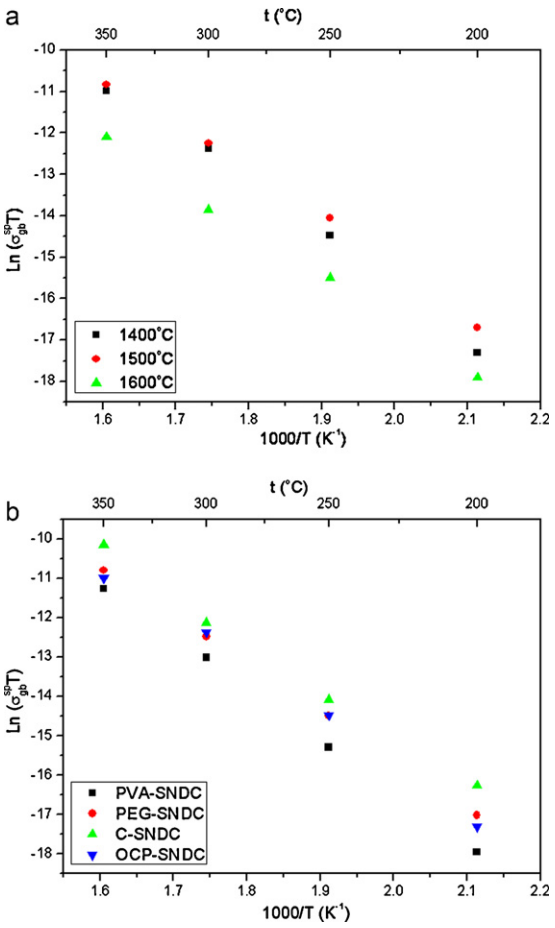

Fig. 8. (a) Specific grain-boundary conductivities for the OCP–SNDC sintered at different temperatures; (b) specific grain-boundary conductivities for the SNDC originated from different processes sintered at 1400 °C.

cations segregating to grain boundaries and SiO_2 contamination at grain boundaries may have significant effect on the grain-boundary conductivities.

Fig. 7 presents the temperature dependence of the conductivity plots for OCP–SNDC sintered at different temperatures. The bulk conductivities do not change much with the variation of the sintering temperatures, indicating the sintering temperature has negligible effect on the bulk conductivities. However, as shown in Fig. 7b, the OCP–SNDC sintered at 1500 °C yields the highest conductivities. Further increase in the sintering temperature leads to much lower grain-boundary conductivities. There is a trade-off relationship between the sintering temperature and the grain-boundary conductivities. On one hand, the high sintering temperature will result in the improvement of the relative density; on the other hand, it might lead to the well developed space charge layer regions, which might decreases the grain-boundary conductivities. In the space charge layer regions, the grain-boundary core is positively charged resulted from the accumulated oxygen vacancies. The oxygen vacancies deplete in the space charge layer regions according to the charge compensation mechanism [21]. In addition, the ordered domain structure existing in the grain boundary also contributes to the conductivity, which is closely associated with the sintering temperature [22]. In the ordering structure domains, the oxygen vacancy ordering reduces the free charge carriers; consequently, the grain-boundary conductivity is lowered. Less ordering domains are assumed to develop in OCP–SNDC sintered at 1500 °C, resulting in higher grain-boundary conductivities than those of other specimens. The optimal sintering temperature is 1500 °C with the highest grain-boundary conductivity values and high relative density of the sintered specimen. The total conductivities reach the highest, indicating the grain-boundary conductivities contribute more than those of the bulk conductivities.

The activation energy E_a can be expressed as follows according to the Arrhenius law:

$$\sigma = \left(\frac{A}{T}\right) \exp\left(\frac{-E_a}{kT}\right) \quad (2)$$

which is shown in Table 1. The activation energy of grain-boundary is much higher than that of the bulk, indicating the total conductivity is mainly determined by the grain boundary. The OCP–SNDC yields the lowest activation energy of bulk and grain boundary, resulting in the lowest activation energy of total conductivity. The

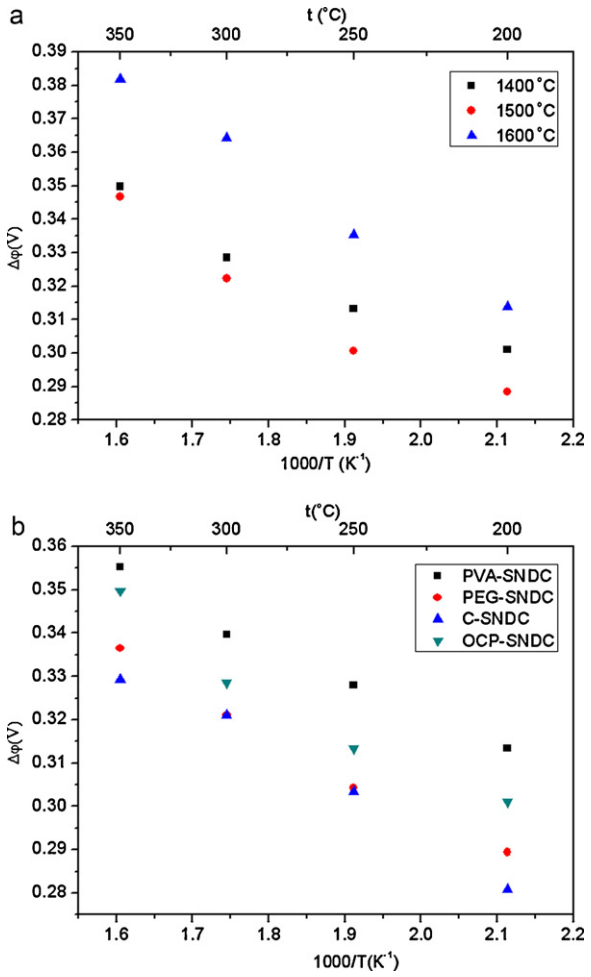

Fig. 9. (a) space charge potentials for the OCP–SNDC sintered at different temperatures; (b) space charge potentials for the SNDC originated from different processes sintered at 1400 °C.

higher relative density and conductivities, lower grain-boundary resistance and activation energy of total conductivity indicate that the OCP–SNDC has superior sinterability and the OCP process is preferable for the synthesis of co-doped ceria electrolyte.

The specific grain-boundary conductivity is commonly utilized to characterize the grain-boundary conduction. Assuming the bulk and grain-boundary permittivity is similar, the specific grain-boundary conductivity can be obtained from Eq. (3) [22].

$$\sigma_{gb}^{sp} = \left(\frac{C_b}{C_{gb}}\right)\sigma_{gb} \tag{3}$$

where C_b is the bulk capacitance and C_{gb} is the grain-boundary capacitance.

The capacitance can be calculated from Eq. (4), where C_i is the bulk or the grain-boundary capacitance, R_i is the bulk or the grain-boundary resistance, Q_i is the pseudocapacitance [22].

$$C_i = \frac{(R_i Q_i)^{1/n}}{R_i} \tag{4}$$

According to the Mott–Schottky model, the ratio of the bulk conductivity to the specific grain-boundary conductivity is given by the Eq. (5) [21]:

$$\frac{\sigma_{\text{bulk}}}{\sigma_{gb}^{sp}} = \frac{\exp(2e\Delta\varphi(0)/k_B T)}{4e\Delta\varphi(0)/k_B T} \tag{5}$$

In Eq. (5), $\Delta\varphi(0)$ is the grain-boundary space charge potential, which is also the Schottky barrier height, e is the elementary electrical charge, k_B is the Boltzmann constant and T is the absolute temperature.

Fig. 8 presents specific grain-boundary conductivities for the OCP–SNDC sintered at different temperatures and for the SNDC originated from different processes. The calculated grain-boundary space charge potentials with sintering temperatures are presented in Fig. 9a. The space charge potentials increase with the increasing temperatures. The lowest space charge potentials are obtained for the OCP–SNDC sintered at 1500 °C, correspondingly, the highest specific grain-boundary conductivities are achieved between 200 °C and 350 °C, as shown in Fig. 8a. The space charge potentials yield the highest values for the OCP–SNDC sintered at 1600 °C, indicating the depletion of oxygen vacancies is more intense at high sintering temperatures. The high sintering temperature results in the formation of nanodomains, which traps the oxygen vacancies and decreases the free charge carriers. Fig. 9b shows the space charge potentials for different specimens. The space charge potentials of PVA–SNDC reach the highest while those of the C–SNDC are the lowest. The variation of the space charge potentials is in accordance with that of specific grain-boundary conductivities, indicating the specific grain-boundary conductivity is principally determined by the space charge potential. The results show that the synthesis process and sintering temperature have great effect on the space charge potential and the specific grain-boundary conductivity.

4. Conclusions

The PVA–SNDC, PEG–SNDC, C–SNDC and OCP–SNDC powders have been successfully synthesized for comparison. The powders form well crystalline structure in good accordance with the cubic fluorite ceria validated by the XRD and HRTEM results. Different morphologies for the powders are observed. The average grain sizes vary with the synthesis process and increase with the increasing sintering temperatures. The bulk conductivities of the sintered samples are quite close while the grain-boundary conductivities of OCP–SNDC are highest. The OCP–SNDC yields the lowest activation energy. The results indicate the OCP–SNDC possesses superior sinterability than those of synthesis processes. The specific grain-boundary conductivity is principally determined by the space charge potential. The synthesis process and sintering temperature have great effect on the space charge potential and the specific grain-boundary conductivity.

Acknowledgements

The authors gratefully acknowledge the financial support from Wallenberg Foundation for the Electron Microscopy measurement in Arrhenius Laboratory, Stockholm University.

References

[1] S.P. Simner, J.F. Bonnett, N.L. Canfield, K.D. Meinhardt, V.L. Sprenkle, J.W. Stevenson, Electrochem. Solid State Lett. 5 (2002) A173–A175.
[2] B.C.H. Steele, Solid State Ionics 129 (2000) 95–110.
[3] H. Inaba, H. Tagawa, Solid State Ionics 83 (1996) 1–16.
[4] S. Omar, E.D. Wachsman, J.C. Nino, Solid State Ionics 178 (2008) 1890–1897.
[5] S. Omar, E.D. Wachsman, J.C. Nino, Solid State Ionics 177 (2006) 3199–3203.
[6] N. Cioatera, V. Parvulescu, A. Rolle, R.N. Vannier, Solid State Ionics 180 (2009) 681–687.
[7] F.Y. Wang, S.Y. Chen, S. Cheng, Electrochem. Commun. 6 (2004) 743–746.
[8] S. Ramesh, V.P. Kumar, P. Kistaiah, C.V. Reddy, Solid State Ionics 181 (2010) 86–91.
[9] S.K. Tadokoro, E.N.S. Muccillo, J. Eur. Ceram. Soc. 27 (2007) 4261–4264.
[10] D.A. Andersson, S.I. Simak, N.V. Skorodumova, I.A. Abrikosov, B. Johansson, Proc. Natl. Acad. Sci. U.S.A. 103 (2006) 3518–3521.

[11] J.S. Ahn, S. Omar, H. Yoon, J.C. Nino, E.D. Wachsman, J. Power Sources 195 (2010) 2131–2135.
[12] T.S. Zhang, J. Ma, Y.Z. Chen, L.H. Luo, L.B. Kong, S.H. Chan, Solid State Ionics 177 (2006) 1227–1235.
[13] W. Zajac, J. Molenda, Solid State Ionics 179 (2008) 154–158.
[14] M. Dudek, A. Rapacz-Kmita, M. Mroczkowska, M. Mosialek, G. Mordarski, Electrochim. Acta 55 (2010) 4387–4394.
[15] S.B. Boskovic, D.R. Djurovic, S.P. Zec, B.Z. Matovic, M. Zinkevich, F. Aldinger, Ceram. Int. 34 (2008) 2001–2006.
[16] W. Kraus, G. Nolze, Federal Institute for Materials Research and Testing: Berlin, Germany, 2000.
[17] R.D. Shannon, Acta Crystallogr. 32 (1976) 751–767.
[18] Y.R. Wang, T. Mori, J.G. Li, J. Drennan, J. Eur. Ceram. Soc. 25 (2005) 949–956.
[19] I.E.L. Stephens, J.A. Kilner, Solid State Ionics 177 (2006) 669–676.
[20] B. Li, Y.Y. Liu, X. Wei, W. Pan, J. Power Sources 195 (2010) 969–976.
[21] X. Guo, R. Waser, Prog. Mater. Sci. 51 (2006) 151–210.
[22] C. Sanchez-Bautista, A.J. Dos Santos-Garcia, J. Pena-Martinez, J. Canales-Vazquez, Solid State Ionics 181 (2010) 1665–1673.